

Reverse time migration and genetic algorithms Combined for Reconstruction in Transluminal Shear Wave Elastography: An In Silico Case Study

Antonio Gomez ^{a,c,*}, Guillermo Rus ^{b,c,d}, Nader Saffari ^a

^a UCL Mechanical Engineering, University College London, Roberts Engineering Building, Torrington Place, London, WC1E 7JE, United Kingdom

^b Department of Structural Mechanics, University of Granada, Edificio Politécnico, Campus de Fuentenueva, Granada, 18071, Spain

^c IBS.GRANADA, Instituto de Investigación Biosanitaria, Avenida de Madrid 15, Granada, 18012, Spain

^d Excellence Research Unit "Modeling Nature", University of Granada, Campus de Fuentenueva, Granada, 18071, Spain

ARTICLE INFO

Keywords:

Image reconstruction
Transluminal elastography
Transurethral elastography
Reverse Time Migration
Genetic algorithms
Prostate cancer
High Intensity Focused Ultrasound

ABSTRACT

A new reconstruction approach that combines Reverse Time Migration (RTM) and Genetic Algorithms (GAs) is proposed for solving the inverse problem associated with transluminal shear wave elastography. The transurethral identification of the first thermal lesion generated by transrectal High Intensity Focused Ultrasound (HIFU) for the treatment of prostate cancer, was used to preliminarily test *in silico* the combined reconstruction method. The RTM method was optimised by comparing reconstruction images from several cross-correlation techniques, including a new proposed one, and different device configurations in terms of the number and arrangement of emitters and receivers of the conceptual transurethral probe. The best results were obtained for the new proposed cross-correlation method and a device configuration with 3 emitters and 32 receivers. The RTM reconstructions did not completely contour the shape of the HIFU lesion, however, as planned for the combined approach, the areas in the RTM images with high level of correlation were used to narrow down the search space in the GA-based technique. The GA-based technique was set to find the location of the HIFU lesion and the increment in stiffness and viscosity due to thermal damage. Overall, the combined approach achieves lower level of error in the reconstructed values, and in a shorter computational time, compared to the GA-based technique alone. The lowest errors were accomplished for the location of HIFU lesion, followed by the contrast ratio of stiffness between thermally treated tissue and non-treated normal tissue. The homologous ratio of viscosity obtained higher level of error. Further investigation considering diverse scenarios to be reconstructed and with experimental data is required to fully evaluate the feasibility of the combined approach.

1. Introduction

The new imaging concept of transluminal shear wave elastography was introduced throughout a collection of articles by Gomez et al. [1–4], with the initial application focusing on prostate cancer detection (see Fig. 1). The transluminal technique uses shear waves that are transmitted directly into the bulk of the tissue by applying oscillatory rotational forces on the luminal wall at a specific location of the lumen length. The transmission produces a pseudo-spherical pattern of shear waves, with arc-shaped vibration of particles (Fig. 2). Shear waves are highly sensitive to changes in the viscoelastic properties of tissue as their speed of propagation depends on the viscoelastic properties of the medium [5]. Reflected waves originate when shear waves encounter a region of altered viscoelastic properties, since these alterations yield changes in the mechanical impedance. Part of this reflected energy reaches back the lumen where shear-sensitive receivers

in contact with the luminal wall measure the vibration amplitude. A preliminary receiver prototype based on bespoke Lead Zirconate Titanate (PZT) piezoelectric blocks (Noliac, Kvistgaard, Denmark) has been patented [6] and initially validated in phantoms [2]. A miniaturised version of the receivers is currently being developed in a parallel study, with dimensions in the order of a $1 \times 1 \times 0.5$ mm per unit receiver. The characteristics of the mechanical contact between the probe and the luminal wall have an impact on the transmission and reception performance. However, these characteristics are application-dependent, and therefore, must be investigated in application-specific experimental studies.

Geometrical and mechanical features of the area of altered viscoelastic properties, including its location, size and change in viscoelastic properties, can be of clinical interest. For example, in cancer detection, as many solid tumours show elevated stiffness compared

* Current address: Department of Structural Mechanics, University of Granada, Edificio Politécnico, Campus de Fuentenueva, Granada, 18071, Spain.

E-mail address: aj.gomez@ucl.ac.uk (A. Gomez).

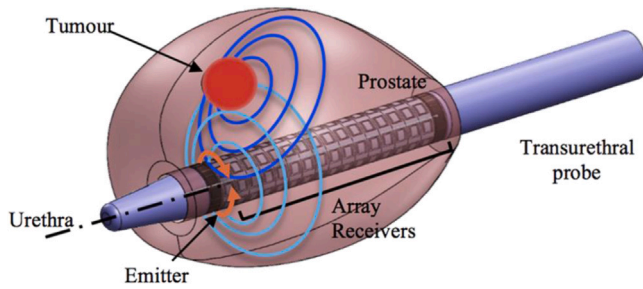


Fig. 1. Conceptual idealisation of the transluminal shear wave elastography technique applied in prostate cancer imaging. The conceptual probe features an emitter and an array of receivers, all enclosed within the prostatic urethra. The emitter's oscillatory rotation generates shear waves transmitted into the tissue, and stiff regions, such as tumours, reflect measurable waves captured by the array of receivers.

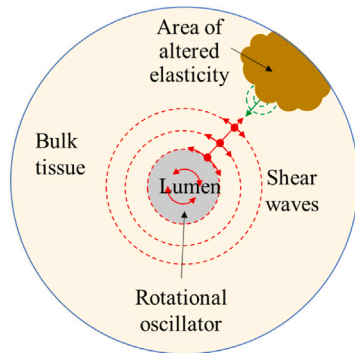


Fig. 2. Wave propagation principle in the transluminal shear wave elastography technique. Shear waves propagate radially from the rotational oscillator. Particles vibrate in an arc-shaped manner perpendicular to the propagation direction. Reflection is generated as the shear waves interact with the area of altered viscoelasticity.

Source: Gomez et al. [3]

to the surrounding non-pathological tissue [5]. The geometrical and mechanical characteristics may be obtained by solving the inverse problem related to the transluminal approach [1]. However, this inverse problem presents limited angle view as the receivers are only located in the luminal cavity. A classical minimisation approach can be used to solve the inverse problem, where a forward model is iteratively compared against the signals collected by the array of receivers. Randomised search methods such as Genetic Algorithms (GAs) have been successfully applied as minimisation methods. Their capacity of dealing with complex problems, and at the same time, their permanent insistence on global convergence is an advantage against other minimisation methods, such as gradient-based methods [7].

In a previous *in silico* feasibility study for the detection of prostate cancer by a transurethral elastography approach, a reconstruction method based on a GA and an elastic forward model, was tested for the reconstruction of the location, diameter and shear modulus μ of a prostate tumour [1]. Nonetheless, soft tissue behaves viscoelastically. Classical viscoelastic rheological models, such as the Kelvin Voigt or Zener models, have been used for modelling the wave propagation of shear waves [8]. Furthermore, fractional viscoelastic models, such as the Kelvin Voigt Fractional Derivative (KVFD), have been proved to model more accurately the velocity dispersion and the frequency-dependent attenuation law of shear waves in elastography [9–11]. A KVFD-based forward model, solved using a Finite Difference Time Domain (FDTD) approach, was developed in a previous work for the transluminal shear wave elastography concept [3]. Compared to the previously used elastic model, the KVFD-based forward model introduces two extra variables: the shear viscosity η and the exponent of the fractional derivative α [3]. Adding more variables to the forward

model increases the number of dimensions of the space of search for the GA-based minimisation method, which leads to a larger computational overhead. A strategy for coping with this can be reducing the size of the search space.

Similar arrangements of receivers and emitters of the transluminal procedure can be found in wave migration imaging. In general terms, migration methods are inversion methods that involve the rearrangement of wave information from time to space domain so that reflection and diffraction are imaged at their true locations [12]. One of the most successful migration methods is Reverse Time Migration (RTM). Although its main application is in geophysics, RTM has also been tested in medical imaging [13]. RTM could be used to find the location of reflectors inside the medium, such as areas of altered viscoelasticity. RTM uses a forward model of the wave propagation, commonly FDTD-based models [14].

RTM has been compared against back projection in medical imaging applications. Liu et al. [13] compared back projection and RTM in *in silico* and *ex vivo* transcranial thermoacoustic tomography. Overall, RTM provided better geometrical accuracy and image quality, nevertheless, results in an *ex vivo* monkey's head showed distorted geometries of inserted needles when using both techniques, due to a selected wave velocity field far from reality according to the authors. A follow-on publication improved the distortion issue by implementing an iterative method that updated the wave velocity field from previous RTM results until the convergence of the output was achieved [15]. Another relevant study of RTM in medical imaging presented a novel approach for optical tomography [14]. The authors obtained high-quality reconstructions from RTM *in silico* tests with sufficient contrast and spatial resolution to achieve inner-structure identification.

The reconstruction problem associated to the transluminal shear wave elastography technique depends on the specific application. Transurethral elastography of the prostate was presented in a previous article as a primary potential application of the transluminal approach [1–4]. Following a similar rationale, transurethral shear wave elastography for the detection of the first High Intensity Focused Ultrasound (HIFU) lesion transrectally generated in the prostate [16,17] is used in this article as a case with potential clinical relevance. Transrectal HIFU thermal ablation is a suitable method for treating localised cancer lesions in the prostate while reducing side-effects [16,17]. The focused ultrasound waves rapidly induce a high increase of temperature to 70–100 °C at the focal area [18], causing tissue coagulation which leads to coagulative necrosis [19]. The stiffness of the treated tissue undergoes a significant increase due to the formation of the thermal lesion [20]. With suggested increments between 5 and 10-fold [21,22], elastography stands as a suitable technique for monitoring the lesion formation. Locating the induced lesion as soon as it appears and monitoring its size are crucial for preventing damage to surrounding healthy tissue, sensitive areas such as the neurovascular bundle and the rectal wall, and also avoiding extra therapy sessions [23].

This article presents a preliminary *in silico* test for the combination of RTM and GAs to serve as a reconstruction technique for transluminal shear wave elastography. A previously developed FDTD forward model is employed in the two reconstruction methods. Identification from the urethra of a HIFU lesion in the prostate is used to test the reconstruction method. First, the adaptation of RTM and GA methods to the transurethral problem is described. Then, several correlation approaches are evaluated for the RTM method. Also, different device configurations, in terms of number of emitters and receivers, are analysed for the RTM method. Finally, the combined approach is tested and compared to using the GA method alone, to reconstruct the location and the increase in stiffness and viscosity of the HIFU lesion.

2. Methods

2.1. Wave propagation model

Both the RTM and the GA-based inversion methods employ a forward model to simulate the propagation of waves. In this study, we

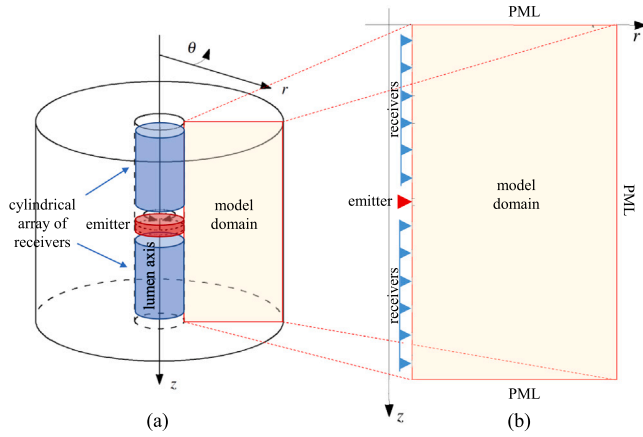


Fig. 3. Geometry and system of coordinates of the wave propagation model. (a) 3D example with one rotational emitter (red disk) and two cylindrical arrays of receivers (blue cylinders), all elements making contact with the luminal wall; source: Gomez et al. [3]. (b) 2D simplified geometry from the 3D case. The luminal wall surface in contact with the receivers is indicated with a distribution of blue triangles.

utilise a forward model specifically developed for transluminal shear wave elastography by our research group, previously described in Gomez et al. [3]. This forward model is governed by a linear viscoelastic KVFD constitutive law (Eq. (1)). According to the KVFD constitutive law, the stress σ depends on the fractional time derivative of order α of the strain ϵ , as shown in the following equation for the shear case (subscript s means shear):

$$\sigma_s = \mu \epsilon_s + \eta_s \frac{\partial^\alpha \epsilon_s}{\partial t^\alpha} \quad (1)$$

where μ is the second Lamé's parameter and η_s is the shear viscosity. Models based on fractional linear viscoelastic constitutive laws, such as the KVFD, can reproduce the power law behaviour of cumulative multiple relaxation processes observed in longitudinal and shear wave propagation in soft tissue [24,25]. Furthermore, fractional viscoelastic models can also reproduce absorption power laws with the exponent taking values from a continuous range from 0 to 2 [10,26,27].

The forward model accounts for axial symmetry and is solved using a FDTD scheme. By considering axial symmetry, the problem is simplified to a 2D scenario, although it should be noted that this assumption poses limitations as it does not fully capture the 3D nature problem, particularly not for the 3D shape of the regions of altered viscoelasticity, thus limiting its realism. Nevertheless, for the purpose of this preliminary investigation, axial symmetry has been deemed acceptable. Moreover, the model can accommodate different number of emitters and receivers (see Fig. 3). The output of the wave propagation model is the time domain readouts from the set of receivers u_{mod} . For further details, the reader is referred to the works by Gomez et al. [3,4].

2.2. Reverse time migration

RTM uses the wave propagation model to *in silico* propagate the excitation event, and the reversed-in-time received signals measured in the experiment. The wave velocity field in the model is set as homogeneous since, in principle, it is unknown. Considering a transluminal probe with M emitters and P receivers, the RTM method follows the procedure below (see scheme in Fig. 4).

1. Experiment: shear waves are generated by the emitter e_m (where $m = 1, 2, 3, \dots, M$) and detected at all P receivers' location, u_{exp} . These signals are acquired by the receivers during sufficiently long time to capture all the multiple reflections from the medium.

2. Forward modelling: the excitation signal used in the experiment is implemented into the wave propagation model at the corresponding location of the emitter e_m . Then, the propagation is simulated and the displacement field in the entire spatial domain $F_m(t, r, z)$ is stored for each time step t_n , with $n = 1, 2, 3, \dots, N$ as the time step index, and N the total number of time steps.
3. Reverse modelling: the signals measured at each receiver, u_{exp} , are reversed in time and implemented as excitation into the wave propagation model at the location of each corresponding receiver. Then, the propagation is simulated and the displacement field in the entire spatial domain $R_m(t, r, z)$ is stored for all time steps t_n .
4. Image correlation $I(r, z)$: cross-correlation of the displacement fields $F_m(t, r, z)$ and $R_m(t, r, z)$ are mathematically processed using element-wise matrix operations. Four of these cross-correlation methods have been previously employed in RTM, as documented in Wang et al. [14]. Additionally, we propose a novel cross-correlation method, which is evaluated alongside the established approaches:

- Original Claerbout cross-correlation method:

$$I_c(r, z) = \sum_{m=1}^M \sum_{n=1}^N F_m(t_n, r, z) R_m(t_n, r, z) \quad (2)$$

- Source illumination method:

$$I_s(r, z) = \sum_{m=1}^M \frac{\sum_{n=1}^N F_m(t_n, r, z) R_m(t_n, r, z)}{\sum_{n=1}^N F_m^2(t_n, r, z)} \quad (3)$$

- Receiver illumination method:

$$I_r(r, z) = \sum_{m=1}^M \frac{\sum_{n=1}^N F_m(t_n, r, z) R_m(t_n, r, z)}{\sum_{n=1}^N R_m^2(t_n, r, z)} \quad (4)$$

- Squared ratio method:

$$I_{ratio^2}(r, z) = \sum_{m=1}^M \frac{\sum_{n=1}^N R_m^2(t_n, r, z)}{\sum_{n=1}^N F_m^2(t_n, r, z)} \quad (5)$$

- Proposed squared illumination method:

$$I_2(r, z) = \sum_{m=1}^M \frac{\sum_{n=1}^N F_m^2(t_n, r, z) R_m^2(t_n, r, z)}{\sum_{n=1}^N F_m^2(t_n, r, z)} \quad (6)$$

where $F_m(t_n, r, z)$ is the displacement field of the forward propagation generated by the m th emitter, $R_m(t_n, r, z)$ is the displacement field of the reverse propagation generated by the m th emitter.

5. Iterative process: Iteration of steps 1–4 for each m combination with transmission from emitter e_m and detection at all the P receivers.
6. Stacking: all the M correlation images are stacked (element-wise matrix addition) to produce the final reconstruction image I .

2.3. Genetic algorithm-based inversion method

An inversion approach, based on the minimisation of the discrepancy between experimental signals u_{exp} and signals obtained from simulations u_{mod} , is tested as the second step of the combined reconstruction method. In general terms, the lower the discrepancy the closer is the model to the experiment. The minimisation is achieved by a GA method [28] adapted from the work by Haataja [29]. The method was previously tested using a elastic forward model [1]. In this case, viscoelasticity is taken into account by using the KVFD wave propagation model as the forward model.

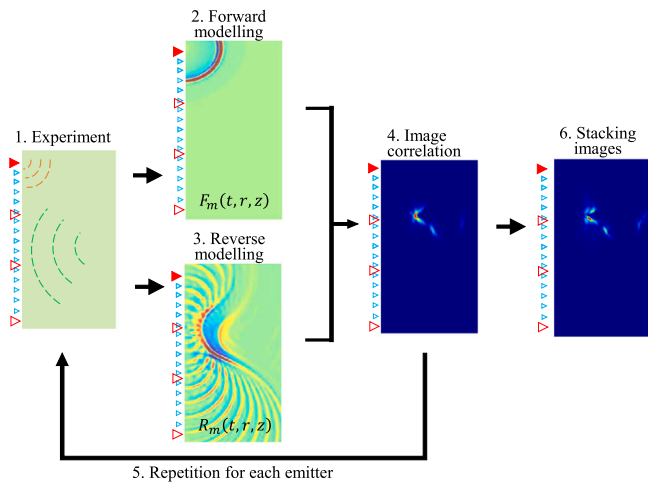


Fig. 4. Steps of the RTM method. Filled red triangles represents the transmitting emitter. Hollow red triangles represents the inactive emitters. Green small triangles represents the distributed array of receivers. (1) Experiment: after transmission of the shear wave, reflections are detected at the array of receivers. (2) The experiment is simulated using a wave propagation model. The displacement field is stored at each spatial and time node, $F_m(t, r, z)$. (3) The recorded signals from the experiment are reversed in time. The reversed signals are inserted into the wave propagation model at the location of their corresponding receiver. The displacement field is stored at each spatial and time node, $R_m(t, r, z)$. (4) Both stored fields, $F_m(t, r, z)$ and $R_m(t, r, z)$, from steps (3) and (4) respectively, are cross-correlated using Eqs. (2)–(6). (5) Steps (1)–(4) are repeated for each emitter. (6) The resulting cross-correlation images from each emitting configuration are stacked to obtain the final RTM image.

Quantification of the discrepancy is measured by a residual vector $R(p)$ defined as the mismatch between u_{exp} and u_{mod} , normalised by the root mean square (RMS) of u_{exp} [30]:

$$R(p) = \frac{u_{exp} - u_{mod}(p)}{RMS(u_{exp})} \quad (7)$$

where p represents the vectorial form of a “chromosome” that contains the set of problem parameters. These problem parameters are the unknown parameters that solve the inverse problem. u_{mod} is the output signals produced by the forward model when is parametrised with a particular chromosome.

A cost function $f^L(p)$ is used to evaluate the fitness of the chromosome as a solution to the inverse problem. $f^L(p)$ is defined as the squared norm of the residual (Eq. (8)), which is also related to the square of the Euclidean distance between the u_{exp} and the u_{mod} signals [28].

$$f^L(p) = \log_{10} \left(\frac{1}{2} |R(p)|^2 + \epsilon \right) \quad (8)$$

with $\epsilon = 10^{-16}$ ensuring the existence of the logarithm [31].

The minimisation of the cost function is iteratively computed by the GA to obtain a chromosome, p_{approx} , that is an approximation to the solution of the inverse problem.

The workflow of the used GA-based inversion method [28] is sketched in Fig. 5. First, an initial solution guess is formed by randomly generating a population of individuals with chromosomes selected from within the expected ranges of each problem parameter. Then, an iterative process is initiated: first, the fitness of each individual as a candidate for the solution is assessed by the cost function $f^L(p)$. Then, the individuals are ranked according to their fitness. A higher probability to survive (i.e. to pass to the next generation of individuals) is given to those with higher fitness. Second, a “crossover” operator allows exchange of part of the chromosome information among individual parents. Finally, during “mutation”, arbitrary parts of the chromosomes are randomly modified to create the next generation of individuals. Other variations and additions can be used, however a basic set of

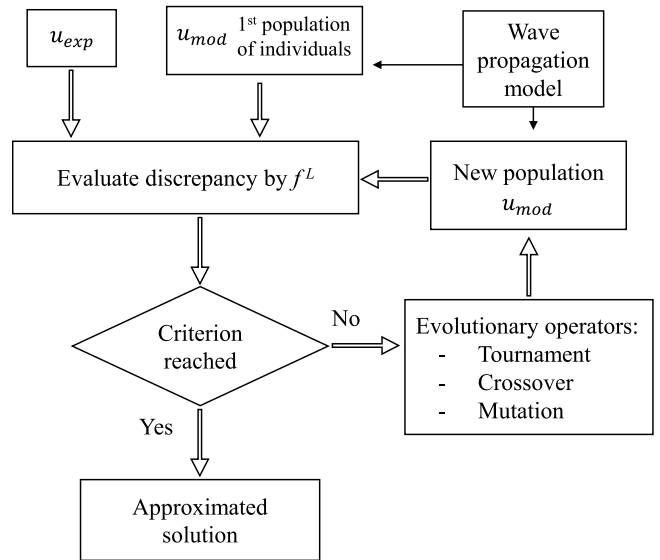


Fig. 5. Steps of the proposed GA-based reconstruction method. The experimental signals u_{exp} are compared against signals generated by the wave propagation model u_{mod} . The input parameters for the model are taken from a range of plausible values. The comparison is made by means of a cost function that evaluates the discrepancy between u_{exp} and u_{mod} . The u_{mod} signals with lower discrepancy to u_{exp} are kept. New other u_{mod} signals are generated after selecting new model parameters using evolutionary operators. These new u_{mod} signals are compared again against u_{exp} . This process is iterated until the end criterion is reached, in this case, a certain number of iterations. The input parameters of the model that produced the u_{mod} signal with the lowest discrepancy to u_{exp} are taken as the solution parameters.

operators was preferred, leaving the search for an optimal configuration for further case-specific work. Finally, the process is iterated until a stop criterion is reached. Given the testing purpose, at a preliminary level, of this study, a specific number of generations was considered acceptable as the stop criterion.

3. Results

The combined approach was initially tested for a case of potential clinical utility: the detection of the first thermal lesion in transrectal HIFU ablation of prostate cancer via the urethra. As mentioned earlier, due to the unavailability of transurethral elastography data from HIFU ablation, an example scenario was simulated using the wave propagation model developed in [3] to produce synthetic data. Consequently, the signals from the receivers u_{exp} are hereafter substituted with their synthetic counterparts obtained through simulation, designated as u_{syn} . Prostate cancer is often multifocal, however, for this preliminary test, a scenario with just one tumour was selected. A Gleason score 7 tumour of 6 mm contained in the posterior side of the prostate was chosen as a tumour with the minimum requirements to be considered clinically relevant. This clinical scenario falls within the category of prostate cancers that are recommended for transrectal HIFU ablation [32]. All the methods were implemented in MATLAB® (Release 2017b, MathWorks, Natick, United States).

3.1. Example case

Transrectal HIFU thermal ablation of prostate cancer is mostly performed using Sonablate® (SonaCare Medical, Charlotte, NC, USA) or Ablatherm® (EDAP TMS, Lyon, France) [16] HIFU systems. In both systems, a transrectal probe is introduced through the rectum. The transducer lens is placed facing the posterior side of the prostate. The ultrasound beam converges at the focal point, raising the temperature of the tissue to a level where irreversible thermal damage occurs [16].

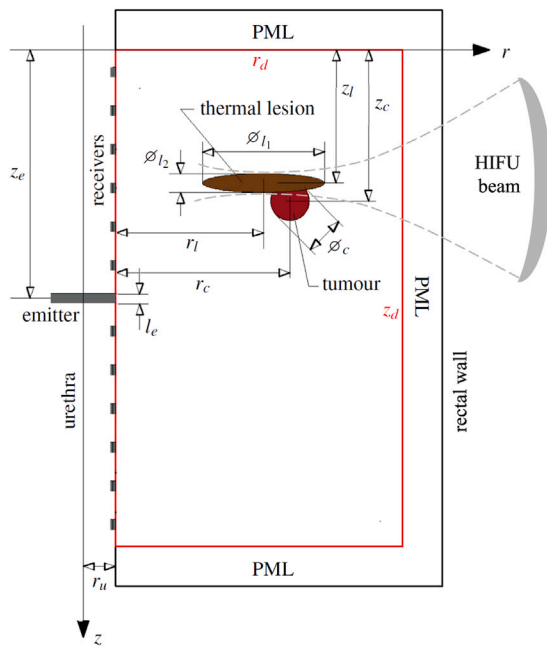


Fig. 6. Scheme of the wave propagation model used to simulate the HIFU ablation scenario. Real spatial domain contoured in red. A Perfectly Match Layer (PML) surrounds the boundary domain with the exception of the urethral wall. Rounded tumour coloured in red, HIFU thermal lesion in brown. Emitter rotating disk and array of receivers in grey on the left side. The HIFU beam that produces the lesion converges from the right side boundary of the domain. This simplified arrangement is, to some extent, representative of the HIFU ablation of prostate cancer from the rectum.

Tissue stiffness varies with temperature [21,22,33]. Collagen denaturation is the responsible for the irreversible stiffness change due to the rise in temperature above 60 °C [34,35]. As temperature increases, the collagen fibres move from their triple helical structure into a randomly coiled configuration [34]. Nonetheless, moderate heat below 60 °C can result in reversible changes, with local unfolding of the collagen fibres and restoration of their native structure when temperature goes back to body temperature [35]. Each HIFU system creates different size ellipsoidal lesions, which are superimposed to cover the tumour. The HIFU Sonablate® system was considered for the example case, which produces lesions of dimension $10 \times 3 \times 3$ mm. The geometrical arrangement of the simulated scenario is represented in Fig. 6 with the values of the model parameters shown in Table 1.

Values of the KVFD parameters (Table 2) for normal and cancerous prostatic tissue with Gleason score 7 were derived from literature data [36,37] and the revision provided in our previous paper [3]. Accordingly, the rounded tumour was modelled as an homogeneous circle with the KVFD parameters defined in Table 2 for cancerous tissue. The changes in the viscoelastic parameters due to ablation are currently unclear and would require further investigation. An estimate of the irreversible increase in stiffness can be approximated from studies for other glandular tissue, such the liver [21,22,33]. According to these, a likely irreversible increase of the shear modulus μ might be between 3 and 6 times. The values of the variation of viscosity η and the degree of the fractional derivative α were kept as those for the cancerous tissue [3] since no suitable data were found in the literature. Therefore, the lesion was modelled as an homogeneous ellipse with the KVFD parameters defined in Table 2 for HIFU thermally ablated tissue.

The excitation signal was implemented as a Gaussian modulated wave with centre frequency of 700 Hz. The recording time was 25 ms, long enough to capture all the reflections generated by the tumour and the HIFU lesion, but not so long as to enhance artefacts due to multiple reflections [38]. Fig. 7 shows three instants of the wave propagation for the pre and post HIFU lesion formation. Reflection was noticeable after

Table 1

Model parameters for the HIFU ablation scenario, based on the work by Gomez et al. [3].

	Description	Value
<i>Spatial dimension of the domain</i>		
r_d	Radial dimension of the domain	20.00 mm
z_d	Depth dimension of the domain	40.00 mm
r_u	Radius of the urethra	3.25 mm
<i>Discretisation parameters</i>		
Δr	r spatial dimension interval	150.00 μm
Δz	z spatial dimension interval	150.00 μm
Δt	Time interval	20.00 μs
t_T	Total time of simulation	25.00 ms
t_L	Time reference for the param. L	1.00 ms
n_{PML}	Number of PML elements	60
<i>General probe setup</i>		
l_e	Length of the disk emitter	1.00 mm
f_e	Centre frequency of the excitation	700 Hz
a_e	Max. amplitude of the excitation	0.30 rad
l_r	Length of each receiver	0.50 mm
<i>Tumour and HIFU lesion geometrical features</i>		
\varnothing_c	Diameter of the tumour	6.0 mm
\varnothing_{l_1}	Major axis of the HIFU lesion	10.0 mm
\varnothing_{l_2}	Minor axis of the HIFU lesion	3.0 mm
r_c	r distance to the tumour centre	15.0 mm
z_c	Depth of the tumour centre	17.0 mm
r_l	r distance to the HIFU lesion centre	14.0 mm
z_l	Depth to the HIFU lesion centre	14.0 mm

Table 2

Values of the KVFD viscoelastic parameters for different type of tissue of the example case.

Source: Gomez et al. [3].

	KVFD parameters		
Type of prostatic tissue	μ (kPa)	η (Pa-s ^α)	α
Normal	3	35	0.35
Cancerous	9	105	0.35
HIFU ablated	15	105	0.35

the wavefront reached the tumour and the HIFU lesion. A general probe setup was chosen for illustration purposes, with one emitter centred in the length of the urethra and 32 receivers distributed along the remaining urethral wall (see Figs. 6 and 7). Fig. 8 shows the measured displacement u_{syn} at each receiver's location for both scenarios. To account for background noise, white noise was added to all the signals measured at the urethral wall, u_{syn} , with an amplitude of 10% of the RMS value of the measured signal with the maximum amplitude among all. This equates to a Signal-to-Noise Ratio (SNR) of 30 dB. Fig. 8 shows the displacement readouts u_{syn} from the receivers with added noise, corresponding to the example shown in Fig. 7.

3.2. RTM results

3.2.1. Comparative study of RTM cross-correlation methods

A comparative study of different cross-correlation methods for the RTM method was carried out. An homogeneous model (i.e. without reflectors) with the same configuration of the example case (Table 1) with the viscoelastic properties of normal prostatic tissue (Table 2) was set as the forward model. The u_{syn} signals were taken from the post first HIFU lesion simulations (Fig. 7d-f). A probe setup with three non-synchronous emitters and 32 receivers was used. The direct wave propagated along the urethral wall was removed from the u_{syn} signals by subtracting the signals recorded in the homogeneous model as performed in Wang et al. [14].

The displacement fields from both forward and reverse modelling were correlated using the proposed five correlation methods. Fig. 9

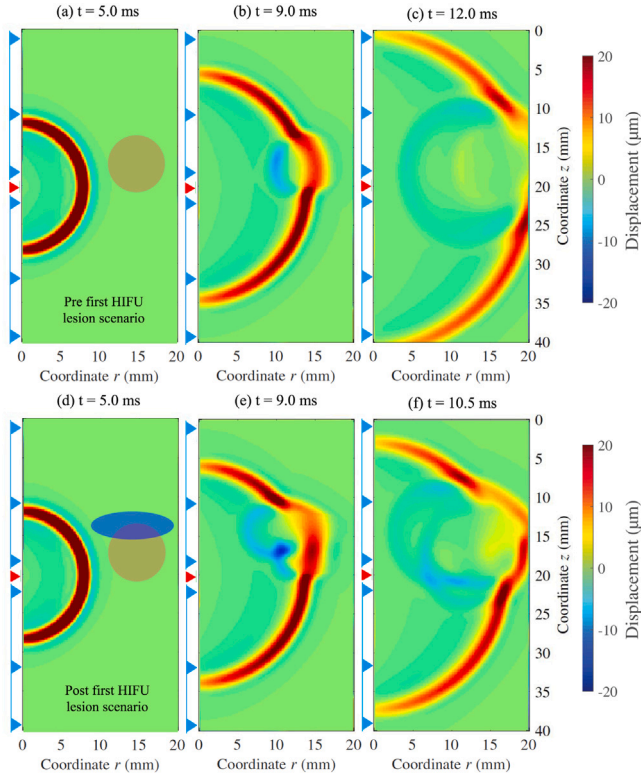


Fig. 7. Example of wave propagation instants for (a–c) a pre first HIFU lesion scenario and (d–f) the corresponding post first HIFU lesion scenario. Rounded tumour of 6 mm in diameter, coloured in brown. Sonablate® lesion in blue. Red triangle shows the emitter's location. Blue triangles show the uniform distribution of receivers.

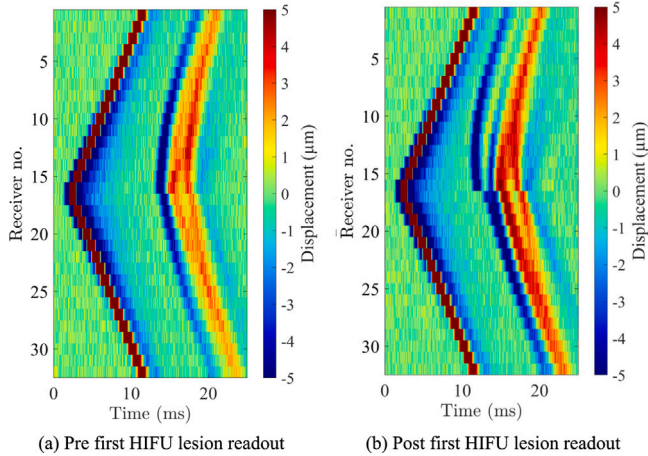


Fig. 8. Displacement readouts (u_{syn}), corresponding to the example shown in Fig. 7, measured at each receiver's location over the total time of simulation for both (a) the pre first HIFU lesion scenario and (b) the post first HIFU lesion scenario. The vertical axis represents the position of each receiver along the urethral wall. The signals contain white noise added with an amplitude of 10% of the RMS value of the signal with the maximum amplitude, which produces a SNR of 30 dB.

shows the resulting image reconstructions. All the images were normalised by adjusting their range, while ensuring that the original zero values remained as zero. As can be observed, none of the methods was able to contour the full shape of the reflectors. Three methods, the new proposed method (Fig. 9c), the Claerhout cross-correlation method (Fig. 9e) and the source illumination method (Fig. 9f), provided some information about the location of the reflectors. Precisely, the three methods highlighted the location of the front side of both reflectors.

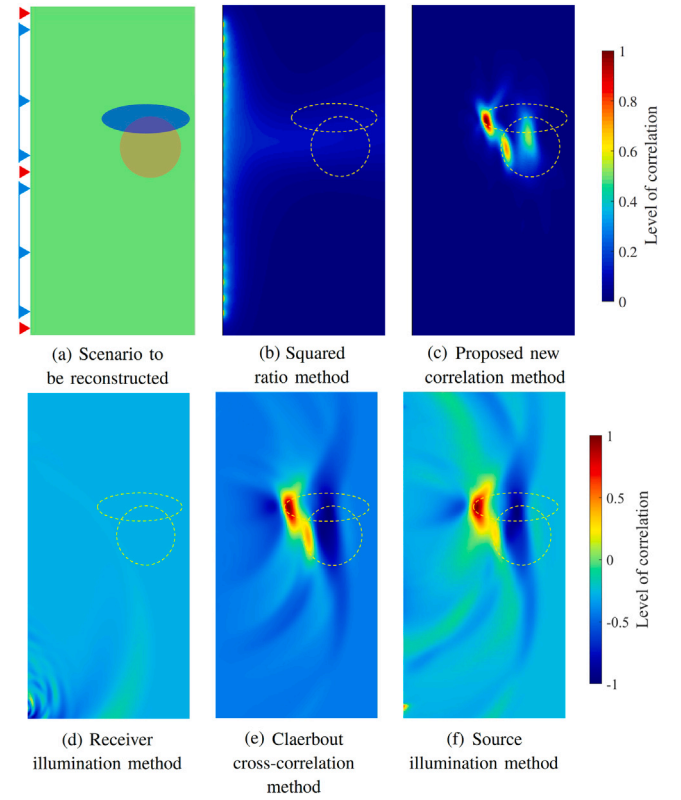


Fig. 9. Comparative analysis of correlation methods for the RTM method. (a) scenario to be reconstructed and the chosen device configuration with three emitters (red triangles) and 32 receivers (blue triangles) uniformly distributed along the urethral wall; (b–f) reconstruction images by using four different correlation methods from the literature (Eqs. (2)–(5)) [14] and the proposed new correlation method (Eq. (6)). Note that the range of the correlation level varies from 0 to 1 in (b) and (c), and from –1 to 1 in (d–f).

Squaring the forward and reverse fields in Eq. (6) made the higher correlation areas in the proposed method appear sharper and with fewer spider-shaped artefacts compared to the Claerhout and source illumination methods. In the three methods, the far side of the reflectors was poorly reconstructed and placed in a slightly anterior region to its actual location. Any of the three methods could be used in the GA-based inversion method to narrow down the region of search. Nonetheless, the new proposed method was chosen to continue this study.

3.2.2. Analysis of the device configuration for RTM

Combinations of emitters and receivers were tested to obtain the most appropriate configuration when using the RTM method with the proposed correlation method (Eq. (6)). The scenario reconstructed was the same as in the previous case (Fig. 7d). 12 device configurations were explored, combining 8, 16 and 32 receivers and 1, 3, 5 and 9 emitters. The model parameters were kept as shown in Tables 1 and 2. Fig. 10 shows the results. Configurations with a higher number of emitters yielded better definition of the shape of reflectors. The same effect was observed when increasing the number of receivers, however, this was not as noticeable as the improvement when increasing the number of emitters. A higher number of receivers reduced the intensity of the spider-shape artefacts observed surrounding the highlighted areas, especially noticeable for the configurations with nine emitters. Regarding the number of receivers, the improvement in definition and the reduction of the artefacts was more significant when using configurations with 16 receivers compared with configurations with 8 receivers, and less noticeable when comparing with configurations with 32 receivers. Considering the device configurations with 32 receivers,

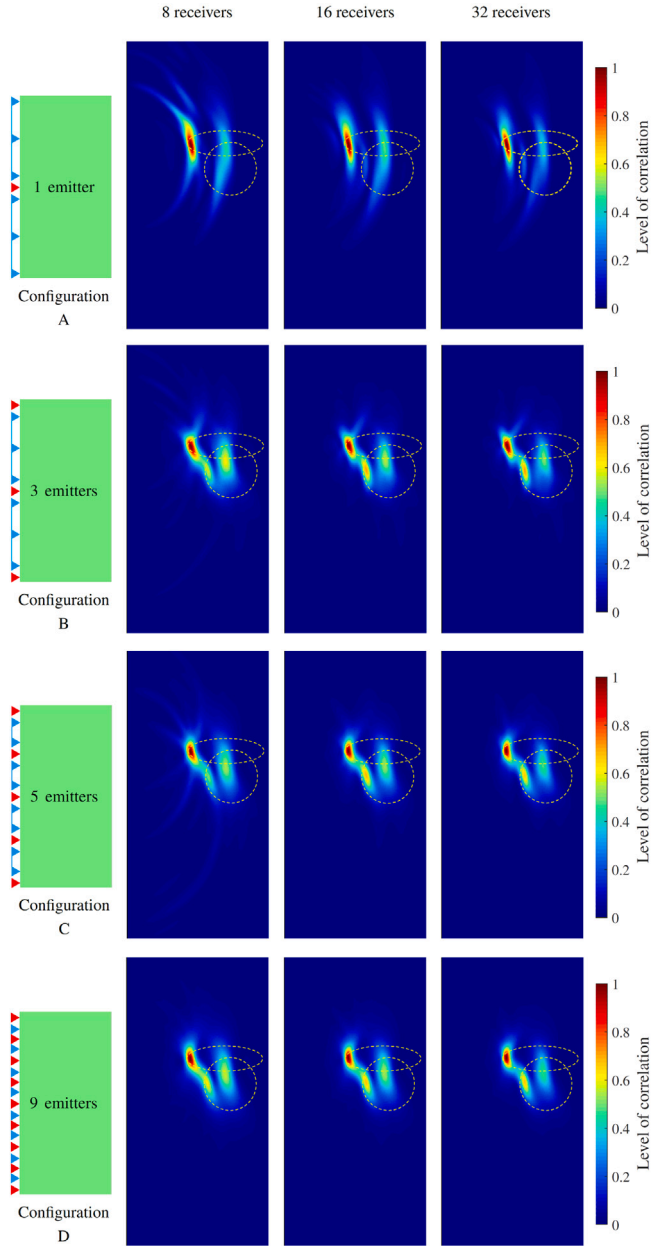


Fig. 10. Comparative analysis of different device configuration for the RTM method, using the proposed correlation method. (a) configuration A with 1 emitter, (b) configuration B with 3 emitters, (c) configuration C with 5 emitters, and (d) configuration D with 9 emitters.

the improvement in the definition of shapes was significant when moving from configuration A to B. It was still noticeable between configurations B and C. However, the improvement was weaker when comparing the configurations C and D.

The number of emitters had a direct impact in the computational overhead, proportionally increasing the computing time by 6 min per additional emitter. The memory required was 2.1 MB, and it barely increased with the number of emitters, since after each image correlation formation (RTM step 5, Fig. 4) the memory used was released. The increase in number of receivers has small influence on either the computation time. Based on the results of the comparative study, and without considering manufacturing challenges or limitations, a balanced optimum device configuration could comprise three emitters and 32 receivers. This device configuration achieved similar results

Table 3

GA parameters.

Parameter	Value
Population of chromosomes	8
Number of generations	50
Evolutionary operator	Value
Probability of mutation	0.3
Probability of crossover	0.8
Tournament probability	0.7
Mutation scale	0.1

Table 4

Lesion parameters and search ranges for the GA method.

Parameter	Real value	Search range
r_{lesion}	14 mm	5–20 mm
z_{lesion}	14 mm	6–28 mm
μ_{ratio}	5	2–6
η_{ratio}	3	2–4

to device configurations C and D with 32 receivers but with shorter computational time.

3.3. Results of the GA-based reconstruction method alone

In this section, the GA-based method is tested to obtain the unknown lesion parameters, with no use of the RTM results from the previous Section 3.2. This serve to later contrast against the combined reconstruction approach. The location, size and viscoelastic properties of the tumour to ablate were assumed to have been previously obtained through a transurethral elastography process (see pre first HIFU lesion scenario in Fig. 7a). The shape and size of the HIFU lesion were assumed fixed as an ellipsoid of dimension $10 \times 3 \times 3$ mm. The position and the viscoelastic properties of the HIFU lesion were the factors to be reconstructed (see Table 1). The viscoelastic properties of the HIFU lesion were defined in terms of the shear modulus contrast ratio, μ_{ratio} , and the shear viscosity contrast ratio, η_{ratio} , relative to the normal surrounding tissue. The vectorial form of a “chromosome”, which contains the factors to be reconstructed, is shown in Eq. (9). The four lesion parameters were considered sufficient to preliminary test the feasibility of the GA-based method. Table 3 show the GA parameters considered, which were optimised after trial-and-error from previous experiences [1,39].

$$p_{lesion} = (r_l, z_l, \mu_{ratio}, \eta_{ratio}) \quad (9)$$

In principle, a larger number of uniformly distributed emitters covers more insonication angles, generating more relevant data for solving the inverse problem. However, the impact of the number of receivers is not fully clear. To investigate this, three different device configurations with 8, 16 and 32 receivers, each with three emitters, were tested in this section.

Table 4 presents the lesion parameters to be reconstructed and their proposed search ranges. The u_{mod} signals were obtained from simulations using the values picked by the GA from the search ranges (Fig. 5). The search range for the centre of the HIFU lesion was defined as a square box with a side length of 25 mm, within which, the HIFU lesion was expected to be located.

The effect of number of receivers was initially studied by evaluating the cost function f_L on two 2D planes with 21^2 evaluation points. The first plane examined the two lesion parameters for the position while maintaining $\mu_{ratio} = 5$ and $\eta_{ratio} = 3$ (see Fig. 12). The second plane explored the two viscoelastic ratios while keeping $r_{lesion} = z_{lesion} = 14$ mm (see Fig. 13).

The absolute minimum of the cost function corresponds to the solution of the inverse problem, representing the actual values of the lesion parameters. After conducting ten simulations for each receiver

Table 5

Cost function at the absolute minimum.

Device conf.	f_{solution}^L	$f_{\text{solution}}^L / f_{\text{mean}}^L$
8 receivers	-2.010 ± 0.140	1.149
16 receivers	-1.899 ± 0.134	1.217
32 receivers	-1.819 ± 0.132	1.262

arrangement, the mean value and standard deviation of the cost function at the solution for the lesion parameters were found to be -2.308 ± 0.009 . No significant differences in these values were observed among different number of receivers. The variability indicated by the standard deviation arose from the random noise added to the u_{syn} signals.

In the $r_{\text{lesion}}-z_{\text{lesion}}$ planes, the absolute minimum of the cost function was clearly located near $r = z = 14$ mm (Fig. 12). However, no absolute minimum was observed in the $\mu_{\text{ratio}}-\eta_{\text{ratio}}$ planes (Fig. 13). Instead, a valley-shape was observed, with its lowest values slightly aligned with $\mu_{\text{ratio}} = 5$. This indicates that viscosity does not have as a significant impact on the reflected signals as elasticity does. In all cases, the valley-shape appears slightly inclined with respect to $\mu_{\text{ratio}} = 5$. The range of values within this inclination includes pairs of values from $\mu_{\text{ratio}} = 5.0 - 5.5$ and $\eta_{\text{ratio}} = 2$, to values of $\mu_{\text{ratio}} = 4.5 - 5.0$, for $\eta_{\text{ratio}} = 4$ (Fig. 13). These pairs of values ($\mu_{\text{ratio}}-\eta_{\text{ratio}}$) produce similar amplitude of the reflected wave due to the presence of the HIFU lesion. Different combinations of μ_{ratio} and η_{ratio} can yield similar reflection coefficients since the reflection coefficient depends on the shear velocity contrast between the lesion and the surrounding tissue, and the shear velocity depends on μ and η (Equations 8–10 in Gomez et al. [4]).

A more precise definition of the absolute minimum is expected to improve the performance of the GA method. Table 5 displays the average value and the standard deviation of the cost function when evaluated in the $r_{\text{lesion}}-z_{\text{lesion}}$ plane for each device configuration. It also includes a comparison with the cost function value at the absolute minimum. The cost function tends to yield higher values outside the absolute minimum when using a larger number of receivers. This results in improved contrast between the absolute minimum and the remaining portion of the $r_{\text{lesion}}-z_{\text{lesion}}$ plane. A similar enhancement in defining the absolute minimum is observed in the configurations with more receivers when comparing $\mu_{\text{ratio}}-\eta_{\text{ratio}}$ planes.

After the cost function analysis, the reconstructed values for the lesion parameters were evaluated. Ten reconstruction tests were carried out for each device configuration using the parameters listed in Table 3. Each test took approximately 9 h on a desktop computer with a quad-core 3.60 GHz processor and 16 GB of RAM.

Table 6 shows the reconstructed values of the four lesion parameters, with the standard deviation providing and indication of the variability in the reconstructed values. The configurations with 16 and 32 receivers offered accurate approximations to the solution of r_{lesion} and z_{lesion} with low variability, while the configuration with 8 receivers exhibited larger variability and less precise approximations. The reconstruction of μ_{ratio} and η_{ratio} was less accurate, regardless of the device configuration, as expected following the analysis of the $\mu_{\text{ratio}}-\eta_{\text{ratio}}$ planes of the cost function.

In summary, the configurations with 16 and 32 receivers produced accurate localisation of the HIFU lesion, with position errors less than one-tenth of a millimetre. The combined reconstruction of μ and η produced shear moduli of 15.85 ± 2.42 kPa and 16.56 ± 2.27 kPa at 700 Hz, for the configurations with 15 and 32 receivers, respectively (calculated using Equations 32–35 from Gomez et al. [3]). This represents averaged errors below 1.0 kPa with SD below 2.4 kPa with respect to the actual shear modulus of the HIFU lesion, 16.72 kPa. These levels of variation for the shear modulus fall within the range of shear modulus values typically observed in prostate cancer [3,4].

The absolute error was determined as the absolute difference between the reconstructed value of each lesion parameter and its actual solution. Relative errors were calculated by scaling the absolute errors

Table 6

Results of the GA-based reconstruction method alone (Rx = receivers).

No. of Rx	Reconstruction results (Mean \pm SD)			
	r_{lesion} (mm)	z_{lesion} (mm)	μ_{ratio}	η_{ratio}
8	14.60 ± 1.20	13.77 ± 0.81	4.55 ± 0.78	2.80 ± 0.60
16	14.06 ± 0.08	14.04 ± 0.18	4.68 ± 0.69	3.27 ± 0.56
32	14.05 ± 0.08	14.04 ± 0.16	4.90 ± 0.65	3.16 ± 0.48
Absolute errors (Mean/ SD)				
	r_{lesion} (mm)	z_{lesion} (mm)	μ_{ratio}	η_{ratio}
8	1.13/0.84	0.68/0.50	0.77/0.54	0.49/0.38
16	0.08/0.06	0.14/0.11	0.56/0.41	0.46/0.35
32	0.08/0.06	0.13/0.10	0.47/0.38	0.42/0.30
Relative errors (Mean/ SD)				
	r_{lesion} (%)	z_{lesion} (%)	μ_{ratio} (%)	η_{ratio} (%)
8	7.50/5.60	3.10/2.29	19.22/13.41	24.50/18.82
16	0.54/0.38	0.63/0.48	14.12/10.35	23.16/17.54
32	0.52/0.38	0.61/0.43	11.77/9.51	21.09/15.01

Table 7

Lesion parameters to be reconstructed and search ranges for the GA in the combined reconstruction approach.

Parameter	Real value	Search range
r_{lesion}	14 mm	12–16 mm
z_{lesion}	14 mm	10–20 mm
μ_{ratio}	5	2–6
η_{ratio}	3	2–4

based on the length of their respective search interval. The lowest relative errors, as shown in Table 6, were consistently below 1.0% for r_{lesion} and z_{lesion} in the 16 and 32-receiver configurations. The configuration with 8 receivers exhibited higher errors with significant variability for the location parameters. Notably, errors in μ_{ratio} and η_{ratio} were consistently larger and displayed more variability compared to the location parameters across all configurations. The highest level of errors was observed in the reconstruction of η_{ratio} .

3.4. Results from the combined reconstruction approach

The combined reconstruction approach used the RTM results to narrow down the spatial search space of the GA-based inversion method. The same clinical scenario (shown in Fig. 7) that was used to test the RTM and the GA-based methods alone was employed to test the combined approach.

The configuration B with three emitters and 32 receivers was used for the RTM part. RTM images were reconstructed from the pre and post first HIFU lesion scenarios. The comparison between RTM images from both pre and post HIFU lesion scenarios helped to estimate that the lesion was produced near the top region where the tumour was located (see Fig. 14). This enabled to narrow down the spatial search box for the GA to an area of 14×13 mm (r and z dimensions respectively). The box was selected manually after visual comparison of the two RTM images. Table 7 shows the revised ranges for the four lesion parameters. Search ranges for μ_{ratio} and η_{ratio} were kept the same as for the study of the GA-based method alone.

For the GA part, a device configuration with a single emitter, placed at the middle section of the prostatic urethra, and 32 receivers, was employed. Fig. 15 shows the value of the cost function in the $r_{\text{lesion}}-z_{\text{lesion}}$ and $\mu_{\text{ratio}}-\eta_{\text{ratio}}$ planes. Compared with the results from the GA-based method alone, the resulting $r_{\text{lesion}}-z_{\text{lesion}}$ plane resembled a zoomed window from the $r-z$ plane shown in Fig. 12. The $\mu_{\text{ratio}}-\eta_{\text{ratio}}$ plane was almost unchanged, since the search ranges of μ_{ratio} and η_{ratio} did not vary. Small differences were due to the random nature of the added white noise.

Ten reconstruction tests were carried out to analyse the performance of the GA reconstruction method after the reduction in the spatial

Table 8

Results of the GA method based on the reduced search domain for 32 receivers.

Reconstruction results (Mean \pm SD)			
r_{lesion} (mm)	z_{lesion} (mm)	μ_{ratio}	η_{ratio}
14.01 \pm 0.04	14.03 \pm 0.07	5.09 \pm 0.13	2.94 \pm 0.52
Absolute errors (Mean/ SD)			
r_{lesion} (mm)	z_{lesion} (mm)	μ_{ratio}	η_{ratio}
0.03/0.03	0.06/0.04	0.13/0.10	0.45/0.33
Relative errors (Mean/ SD)			
r_{lesion} (%)	z_{lesion} (%)	μ_{ratio} (%)	η_{ratio} (%)
0.22/0.17	0.26/0.20	3.25/2.50	22.54/16.50

search domain. Setting parameters of the GA were maintained as shown in Table 3. Table 8 displays the reconstructed values for the four lesion parameters. Results for r_{lesion} and z_{lesion} were significantly close to the actual values (see Table 7). The reduction in the search domain yielded a slightly more accurate approximation of the location parameters. μ_{ratio} and η_{ratio} were less accurately reconstructed compared with the location parameters. Errors in the reconstruction of the location parameters were similar to using the GA-based method alone. However, an improvement from 10% to 2.5% in the level of error for μ_{ratio} with lower variability was accomplished. The error in the reconstruction of η_{ratio} did not decrease significantly.

The performance of the GA method, with and without reducing the spatial search domain, is analysed in Fig. 16. The combination approach shows better performance, achieving lower values of the cost function in fewer generations and with reduced variability. This improved convergence speed may explain the better reconstruction of μ_{ratio} , as the GA can focus on finding more accurate approximations.

4. Discussion

In this article, a reconstruction approach based on the combination of two independent methods, a RTM method and a GA-based inversion technique, applied to the medical imaging concept of transluminal shear wave elastography, has been tested *in silico*. The novel imaging concept was introduced in previous work [1–3], which includes the development of a forward model for transluminal wave propagation based on a fractional viscoelastic constitutive law, along with its experimental validation [3,4]. Experimental evidence of wave propagation and detection at the luminal wall using a preliminary transluminal array of piezoelectric receivers was also accomplished [2]. While an initial attempt to reconstruct mechanical parameters using a GA-based inversion method was made in Gomez et al. [1], the forward model relied on a pure elastic constitutive law, which is not representative of the viscoelastic behaviour of soft tissue. In this article, the GA-based method, combined with information from prior RTM reconstructions, was employed, taking advantage of a fractional viscoelastic forward model developed previously [3]. The same fractional viscoelastic forward model was also used in the RTM method.

RTM was introduced for the first time in seismology by Whitmore [40], however, it was not until two decades ago that RTM became a practical method due to its demanding computational requirements. Although RTM has found major applications in hydrocarbon exploration [41], it has also been utilised in other fields, such as non-destructive evaluation, particularly crack detection using ultrasound [42], and in locating embedded elements within concrete [38]. To the best of the authors' knowledge, this article marks the pioneering application of RTM in the field of elastography.

Localisation and evaluation of the viscoelastic properties of a single HIFU lesion in the ablation of prostate cancer was used for illustrating and testing the two reconstruction methods. The stiffness of the tissue undergoes an irreversible increase due to the HIFU lesion formation,

which based on previous studies [20,21,23,43,44], could serve to measure the thermal damage. It is important to note that the biological state and the extent of the necrotic lesion will naturally evolve over time post-treatment, as part of the healing processes [18]. This evolution will undoubtedly influence the tissue stiffness values and their spatial distribution within the gland, which, at present, remains uncertain.

No experimental data was available at the time of writing this article. Therefore, the wave propagation model developed by the authors [3] was employed to generate *in silico* data. White noise was artificially added to achieve a SNR of 30 dB. This model was based on a KVFD constitutive law, a suitable linear viscoelastic model for simulating shear wave propagation in elastography applications [24]. The model provided readings from an array of receivers located at the urethral wall (see Fig. 6). The model allowed for the creation of regions with altered KVFD properties to simulate a round tumour with a 6 mm diameter and a Gleason score of 7, as well as a first HIFU lesion produced according to the Sonablate® HIFU platform.

The KVFD parameters chosen for the tumour and the HIFU lesion were compiled from previous articles, as indicated in Gomez et al. [3]. The surrounding tissue may also exhibit altered mechanical properties to some extent. Additionally, thermal doses overlapping could lead to different mechanical properties than a single dose. Studies addressing these aspects were not found in the literature.

Another assumed limitation of the wave propagation model is its 2D axisymmetric simplification, resulting in toroidal-shaped inclusions that are not representative of real scenarios [3,4]. In a real situation with a functional cylindrical array of receivers in the transluminal probe, signals from the entire 3D volume would reach the receivers. This out-of-plane information would introduce complexity to the inverse problem. The wave propagation model considered only attenuation due to absorption and geometrical diffraction. In a real scenario, more significant attenuation can be expected, resulting from scattering in addition to energy loss mechanisms. For the purpose of this preliminary work, the settings of the wave propagation model were deemed suitable. However, it is advisable to address the limitations mentioned above to achieve more realistic simulations.

The RTM method was tested using five different cross-correlation methods, three of which successfully identified the region containing the reflectors, namely the HIFU lesion and the tumour. These three methods included the Claerbout method, the source illumination method and a new proposed one. Among them, the new proposed method exhibited lower level of artefacts. This information is valuable for estimating the extent of the thermally treated region when the placement of the HIFU beam is accurately known. It is worth noting the presence of what appeared to be a shifted back side location of the reflectors, a phenomenon dependent on frequency and transmit conditions, which merits further investigation.

Several device configurations, varying in the number of emitters and receivers, were tested. The number of emitters ranged from 1 to 9, while the number of receivers was fixed at 8, 16 and 32. Both emitters and receivers were uniformly distributed along the length of the lumen wall. Results showed that having 3 or more emitters effectively contoured the shape of the front side of the reflectors. Furthermore, an increased number of receivers helped reduce spider-shape artefacts. However, it is important to note that the number of emitters directly influenced the computational time, as each additional emitters required running the RTM algorithm one more time. As a result, a device configuration with three emitters and 32 receivers was chosen as the most balanced configuration for this preliminary test. For the sake of brevity and given the preliminary nature of this work, further enhancements to the method are left for future investigation.

The method for obtaining the initial wave velocity field for the homogeneous model was not examined in this study. Further exploration could consider basic concepts, such as the iterative method proposed by Liu [15]. Additionally, by using a higher frequency excitation, shorter wavelengths would be generated, potentially improving the

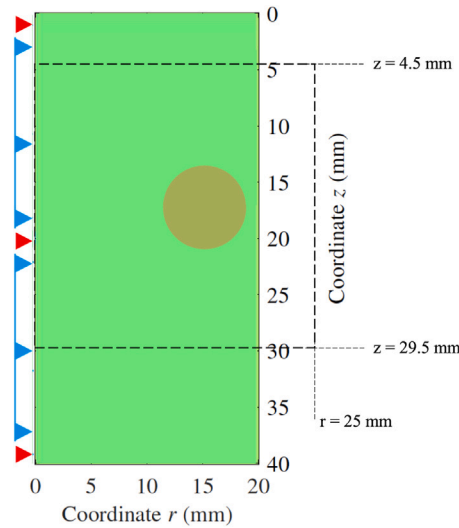


Fig. 11. Scenario for generating the u_{mod} signals. The dashed square represents a box of 25×25 mm, within which the HIFU lesion is expected to have been formed. Table 4 shows the range of possible values for the r and z coordinates of the centre of the lesion.

reconstruction of the contour of the HIFU lesion. Furthermore, various techniques from the literature can be employed to enhance RTM reconstruction in lossy viscoelastic media, including methods to compensate for amplitude losses, such as amplitude compensation, inverse filtering, and inverted-loss medium methods [14,45,46]. The definition of the reflectors shape can also be improved through iterative process, such as the one proposed by Liu [15], which updates the wave velocity field from previous RTM results until convergence of the final image. Finally, in addition to cross-correlation, other estimators for the RTM method could be explored, such as phase-shift [47] or variance-based methods [48].

Prior to evaluating the combined reconstruction approach, the GA-based inversion method was independently tested. Four lesion parameters were defined as the solution to the inverse problem: the two coordinates for the lesion centre, r_l and z_l , and the elasticity and viscosity contrast ratios between treated and normal tissue, μ_{ratio} and η_{ratio} , respectively. The search space for the location parameters consisted of a 25×25 mm box within which the HIFU lesion was expected to have been formed, assuming that the location of the HIFU probe can be estimated to some extent (see Fig. 11). The cost function defined for the inverse problem (Eq. (8)) was evaluated in a 4D space comprised of the four lesion parameters. The global minimum of the cost function was well defined with respect to the location parameters (see Fig. 12) and μ_{ratio} (see Fig. 13). In contrast, it was not clearly defined for η_{ratio} (see Fig. 13), which resulted in a limited sensitivity of the GA in finding its solution. Alternative cost function definitions that could enhance sensitivity to the viscosity ratio η_{ratio} may be explored in future work.

The results from the reconstruction tests are presented in Table 6. The GA-based inversion method alone yielded reconstructions with low error levels for the location parameters. While μ_{ratio} and η_{ratio} exhibited higher reconstruction errors, these results are still considered valuable from a clinical perspective. An additional comparison was conducted to assess how the number of receivers affected the performance of the GA-based inversion method. The largest error levels were observed with 8 receivers, while almost identical error levels were found for configurations employing 16 and 32 receivers.

A single GA reconstruction required approximately 9 h on a standard desktop computer. Improvements in computational efficiency could be achieved by employing a high-performance computing system equipped with multiple CPU cores and GPU computing capability. The optimisation of the algorithms is integral to the future plan for

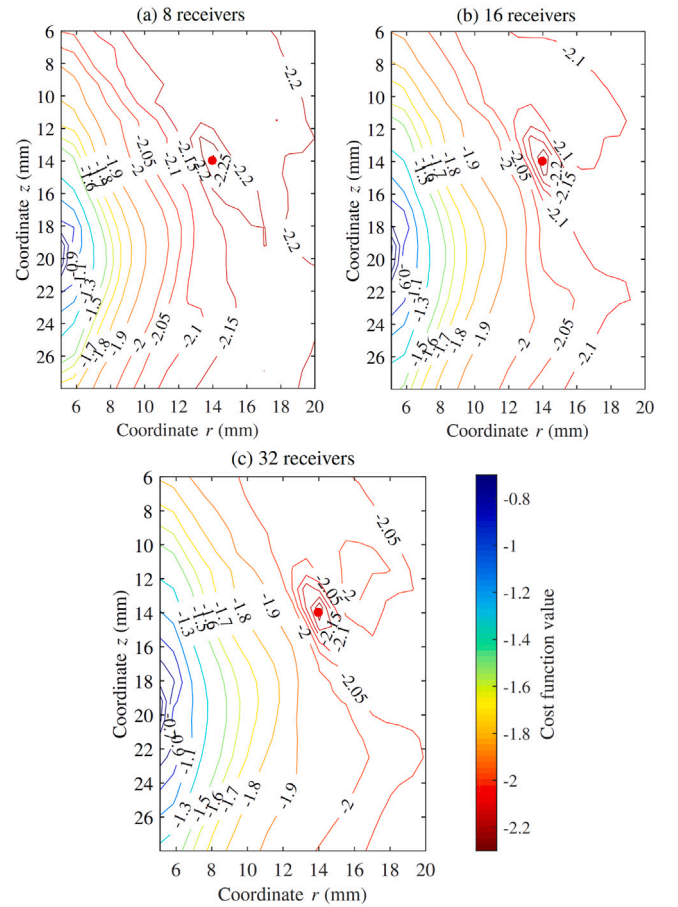


Fig. 12. r_{lesion} - z_{lesion} planes from the evaluation of the cost function. The r_{lesion} and z_{lesion} parameters of the solution to the inverse problem are marked as red dots at $r = z = 14$ mm.

continuation. In a practical scenario, the target computation time is envisioned to span from near-real-time processing to a maximum of 24 h.

The reconstruction approach, combining RTM and GA, was tested with the search space for the GA reduced by 70% after utilising the previous RTM reconstruction images. Fig. 14 illustrates the reduced search box. Upon comparison with the GA-based inversion method used in isolation, there was not significant improvement in the accuracy of reconstructing the location parameters. However, this was not the case for the μ_{ratio} parameter, as its reconstruction error improved from 11% to 2%. It is possible that the RTM images can serve to expedite the GA inversion by terminating the minimisation process in fewer generations or enhancing the accuracy of reconstructing specific parameters.

Table 2 displays the selected KVFD viscoelastic parameters for testing. It should be noted that additional viscoelastic value ranges will be necessary for an expanded analysis, as changes in elasticity and viscosity may vary depending on the region of the prostate and the presence of other pathologies, such as Benign Prostatic Hyperplasia (BPH) [49]. In-depth assessment of the performance of the combined methods will require various combinations of elasticity and viscosity ranges for both normal and cancerous tissue. Furthermore, multiple scenarios involving different lesion locations, sizes, and shapes should also be examined.

Besides the inherent limitations of the transurethral application, practical aspects of the technique may introduce further constraints. These include the nonlinear response of tissue to probe compression, the potential for probe movement during data acquisition, and the presence of the transurethral probe within the HIFU field, among others.

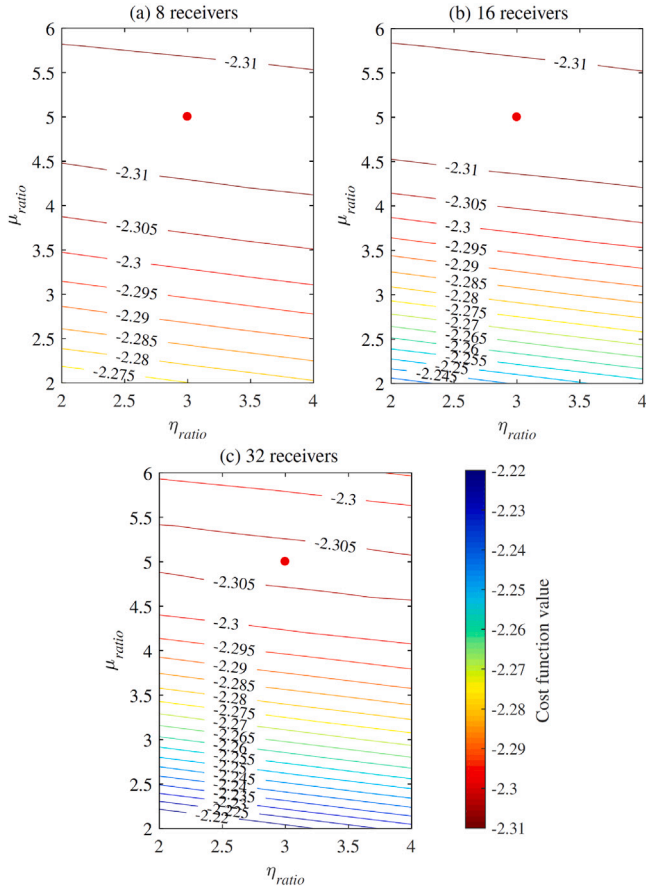


Fig. 13. μ_{ratio} - η_{ratio} planes from the evaluation of the cost function. The μ_{ratio} and η_{ratio} parameters of the solution to the inverse problem are marked as red dots at $\mu_{ratio} = 5$ and $\eta_{ratio} = 3$.

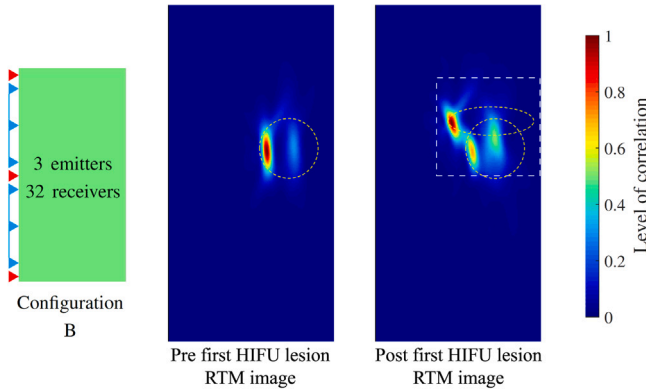


Fig. 14. RTM images for the pre and post first HIFU lesion situations used to test the combined reconstruction approach, using the proposed RTM correlation method (Eq. (6)) and the device configuration B with 32 receivers (Fig. 10). The area where the HIFU lesion was suspected is contoured with a dashed line.

Addressing these limitations will be a crucial aspect of the ongoing development of the transurethral shear wave elastography technique.

5. Conclusions

A novel reconstruction approach, combining the use of both RTM method and a GA-based inversion technique, has been proposed to address the inverse problem associated with transluminal shear wave elastography. This approach was tested through preliminary *in silico*

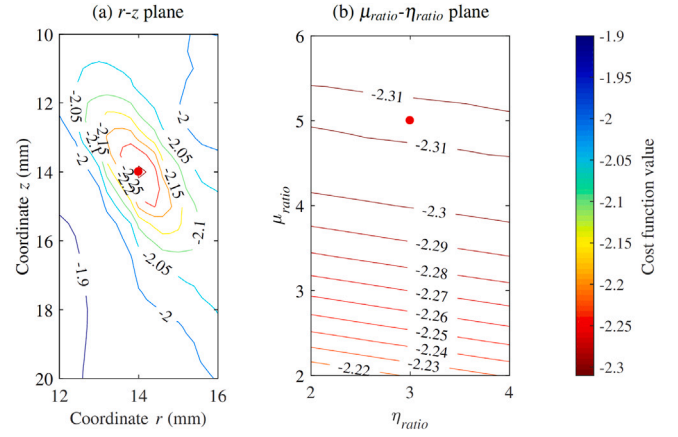


Fig. 15. (a) r - z and (b) μ_{ratio} - η_{ratio} planes from the evaluation of the cost function in the reduced search space. The parameters of the real HIFU lesion are marked as red dots.

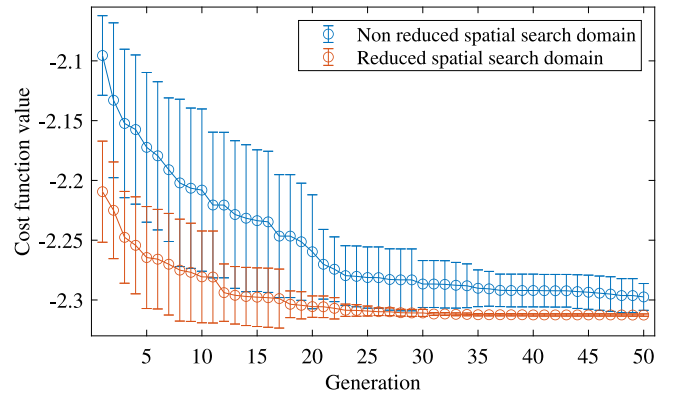


Fig. 16. Cost function value of the best chromosome over the number of generations, with and without reduction of the spatial search domain for the GA, i.e., the combined reconstruction approach or the GA-based method alone, respectively. Data is shown in terms of mean and standard deviation values.

experiments, specifically adapted for the transurethral application in detecting the initial HIFU lesion for prostate cancer treatment.

The RTM method was enhanced by introducing a new cross-correlation method and employed a device configuration with 3 emitters and 32 receivers. The RTM reconstructions were instrumental in providing information on the potential location and extent of the region where the HIFU lesion may have developed.

The combined reconstruction leveraged the results from the RTM method to refine the search space for the GA-based reconstruction of four essential lesion parameters: the coordinates of the centre of the lesion and the contrast ratio for both shear modulus and shear viscosity between treated and untreated tissue. The results demonstrated the highest accuracy for the location of HIFU lesion, followed by the contrast ratio for tissue stiffness, while the viscosity ratio showed the greatest level of error.

Further comprehensive investigations are necessary, encompassing diverse scenarios and incorporating experimental data, to meticulously assess the performance and capabilities of this combined reconstruction approach.

Declaration of competing interest

The authors declare that they have no known competing financial interests or personal relationships that could have appeared to influence the work reported in this paper.

Data availability

Data will be made available on request.

Acknowledgements

The first author was supported by a Talentia scholarship C2012H-75146405T-1 from the regional government of Andalusia, Spain, for his PhD programme at University College London, United Kingdom. Other minor financial support was provided by the Ministry of Science and Innovation, Spain, grants PID2020-115372RB-I00 and PDC2021-120945-I00, by the regional government of Andalusia, Spain, grants B-TEP-026-UGR18 and P18-RT-1653, and by University of Granada PPJIA2022-22.

References

- [1] A. Gomez, G. Rus, N. Saffari, Use of shear waves for diagnosis and ablation monitoring of prostate cancer: a feasibility study, *J. Phys. Conf. Ser.* 684 (2016) 012006, <http://dx.doi.org/10.1088/1742-6596/684/1/012006>.
- [2] A. Gomez, M. Hurtado, A. Callejas, J. Torres, N. Saffari, G. Rus, Experimental evidence of generation and reception by a transluminal axisymmetric shear wave elastography prototype, *Diagnostics* 4 (11) (2021) 645, <http://dx.doi.org/10.3390/diagnostics11040645>.
- [3] A. Gomez, G. Rus, N. Saffari, Wave propagation in a fractional viscoelastic tissue model: Application to transluminal procedures, *Sensors* 8 (21) (2021) 2778, <http://dx.doi.org/10.3390/s21082778>.
- [4] A. Gomez, A. Callejas, G. Rus, N. Saffari, Experimental evidence of shear waves in fractional viscoelastic rheological models, *Sci. Rep.* 12 (2022) 7448, <http://dx.doi.org/10.1038/s41598-022-11490-4>.
- [5] D. Cosgrove, F. Piscaglia, J. Bamber, J. Bojunga, J.-M. Correia, O.H. Gilja, A.S. Klausner, I. Sporea, F. Calliada, V. Cansiani, M. D'Onofrio, E.E. Drakonaki, M. Fink, M. Friedrich-Rust, J. Fromageau, H.R. F., C. Jenssen, R. Ohlinger, R. Saftoiu, F. Shaefer, C.F. Dietrich, EFSUMB guidelines and recommendations on the clinical use of ultrasound elastography. Part 2: Clinical applications, *Ultraschall Med.* 34 (3) (2013) 238–253, <http://dx.doi.org/10.1055/s-0033-1335375>.
- [6] N. Saffari, G. Rus, A. Gomez, E. Sanchez, Transluminal device and procedure for the mechanical characterization of structures, in: Patent no. ES2687485A1 - PCT/ES2018/070243, 2018.
- [7] G. Rus, S.Y. Lee, S.Y. Chang, S.C. Wooh, Optimized damage detection of steel plates from noisy impact test, *Internat. J. Numer. Methods Engrg.* 68 (7) (2006) 707–727, <http://dx.doi.org/10.1002/nme.1720>.
- [8] M. Orescanin, Y. Wang, M.F. Insana, 3-D FDTD Simulation of Shear Waves for Evaluation of Complex Modulus Imaging, *IEEE Trans. Ultrason. Ferroelectr. Freq. Control* 58 (2) (2011) 389–398, <http://dx.doi.org/10.1109/TUFFC.2011.1816>.
- [9] M. Caputo, J.M. Carcione, F. Cavallini, Wave simulation in biologic media based on the Kelvin-Voigt fractional-derivative stress-strain relation, *Ultrasound Med. Biol.* 37 (6) (2011) 996–1004, <http://dx.doi.org/10.1016/j.ultrasmedbio.2011.03.009>.
- [10] S. Holm, S.P. Näsholm, Comparison of fractional wave equations for power law attenuation in ultrasound and elastography, *Ultrasound Med. Biol.* 40 (4) (2014) 695–703, <http://dx.doi.org/10.1016/j.ultrasmedbio.2013.09.033>.
- [11] W. Zhang, S. Holm, Estimation of shear modulus in media with power law characteristics, *Ultrasonics* 64 (2016) 170–176, <http://dx.doi.org/10.1016/j.ultras.2015.09.003>.
- [12] R.E. Sheriff, *Encyclopedic Dictionary of Applied Geophysics*, fourth ed., Society of Exploration Geophysicists, 2012.
- [13] Z. Liu, L. Liu, Y. Xu, L.V. Wang, Transcranial thermoacoustic tomography: a comparison of two imaging algorithms, *IEEE Trans. Med. Imaging* 32 (2) (2013) 289–294, <http://dx.doi.org/10.1109/TMI.2012.2224667>.
- [14] Z. Wang, H. Ding, G. Lu, X. Bi, Reverse-time migration based optical imaging, *IEEE Trans. Med. Imaging* 35 (1) (2016) 273–281, <http://dx.doi.org/10.1109/TMI.2015.2469598>.
- [15] Z. Liu, L. Liu, Application of iterative reverse time migration procedure on transcranial thermoacoustic tomography imaging, in: *Soundscape Semiot. - Localization Categ.*, InTech, 2014, pp. 47–64, <http://dx.doi.org/10.5772/56619>.
- [16] S. Guillaumier, M. Peters, M. Arya, N. Afzal, S. Charman, T. Dudderidge, F. Hosking-Jervis, R.G. Hindley, H. Lewi, N. McCartan, C.M. Moore, R. Nigam, C. Ogden, R. Persad, K. Shah, J. van der Meulen, J. Virdi, M. Winkler, M. Emberton, H.U. Ahmed, A multicentre study of 5-year outcomes following focal therapy in treating clinically significant nonmetastatic prostate cancer, *Eur. Urol.* (74) (2018) 422–429, <http://dx.doi.org/10.1016/j.eururo.2018.06.006>.
- [17] A. Bakavicius, G. Marra, P. Macek, C. Robertson, A.L. Abreu, A.K. George, B. Malavaud, P. Coloby, P. Rischmann, M. Moschini, A.R. Rastinehad, A. Sidana, A. Stabile, R. Tourinho-Barbosa, J. de la Rosette, H. Ahmed, T. Polascik, X. Cathelineau, R. Sanchez-Salas, Available evidence on HIFU for focal treatment of prostate cancer: a systematic review, *Int. Braz. J. Urol.* 2 (48) (2022) 263–274.
- [18] C. Chaussy, D. Tilki, S. Thüroff, Transrectal high-intensity focused ultrasound for the treatment of localized prostate cancer: Current role, *J. Cancer Ther.* 04 (04) (2013) 59–73, <http://dx.doi.org/10.4236/jct.2013.44A007>.
- [19] G. ter Haar, Intervention and therapy, *Ultrasound Med. Biol.* 26 (00) (2000) s51–s54, [http://dx.doi.org/10.1016/s0301-5629\(00\)00164-2](http://dx.doi.org/10.1016/s0301-5629(00)00164-2).
- [20] B. Arnal, M. Pernot, M. Tanter, Monitoring of thermal therapy based on shear modulus changes: I. Shear wave thermometry, *IEEE Trans. Ultrason. Ferroelectr. Freq. Control* 58 (2) (2011) 369–378, <http://dx.doi.org/10.1109/TUFFC.2011.1814>.
- [21] E. Sapin-de Brosses, J.L. Gennisson, M. Pernot, M. Fink, M. Tanter, Temperature dependence of the shear modulus of soft tissues assessed by ultrasound, *Phys. Med. Biol.* 55 (2010) 1701–1718, <http://dx.doi.org/10.1088/0031-9155/55/6/011>.
- [22] A. Mariani, W. Kwiecinski, M. Pernot, D. Balvay, M. Tanter, O. Clement, C.a. Cuenod, F. Zinzindohoue, Real time shear waves elastography monitoring of thermal ablation: in vivo evaluation in pig livers, *J. Surg. Res.* 188 (1) (2014) 37–43, <http://dx.doi.org/10.1016/j.jss.2013.12.024>.
- [23] L. Curiel, R. Souchon, O. Rouvière, A. Gelet, J.Y. Chapelon, Elastography for the follow-up of high-intensity focused ultrasound prostate cancer treatment: Initial comparison with MRI, *Ultrasound Med. Biol.* 31 (11) (2005) 1461–1468, <http://dx.doi.org/10.1016/j.ultrasmedbio.2005.06.013>.
- [24] S. Holm, *Waves with Power-Law Attenuation*, Springer, Switzerland, 2019.
- [25] K.J. Parker, T. Szabo, S. Holm, Towards a consensus on rheological models for elastography in soft tissues, *Phys. Med. Biol.* 64 (21) (2019) <http://dx.doi.org/10.1088/1361-6560/ab453d>.
- [26] W. Chen, S. Holm, Modified Szabo's wave equation models for lossy media obeying frequency power law, *J. Acoust. Soc. Am.* 114 (5) (2003) 2570–2574, <http://dx.doi.org/10.1121/1.1621392>.
- [27] S. Holm, S.P. Näsholm, A causal and fractional all-frequency wave equation for lossy media, *J. Acoust. Soc. Am.* 130 (4) (2011) 2195, <http://dx.doi.org/10.1121/1.3631626>.
- [28] R. Gallego, G. Rus, Identification of cracks and cavities using the topological sensitivity boundary integral equation, *Comput. Mech.* 33 (2) (2004) 154–163, <http://dx.doi.org/10.1007/s00466-003-0514-4>.
- [29] J. Haataja, *Matlab Function for Simulating a Simple Real-Coded Genetic Algorithm*. Center for Scientific Computing, Box 405, FIN-0210, juha.haataja@csc.fi. Tech. Rep., 2000.
- [30] J. Melchor, G. Rus, Torsional ultrasonic transducer computational design optimization, *Ultrasonics* 54 (7) (2014) 1950–1962, <http://dx.doi.org/10.1016/j.ultras.2014.05.001>.
- [31] R. Palma, G. Rus, R. Gallego, Probabilistic inverse problem and system uncertainties for damage detection in piezoelectrics, *Mech. Mater.* 41 (9) (2009) 1000–1016, <http://dx.doi.org/10.1016/j.mechmat.2009.05.001>.
- [32] H.U. Ahmed, R.G. Hindley, L. Dickinson, A. Freeman, A.P. Kirkham, M. Sahu, R. Scott, C. Allen, J. Van der Meulen, M. Emberton, Focal therapy for localised unifocal and multifocal prostate cancer: a prospective development study, *Lancet Oncol.* 13 (6) (2012) 622–632, [http://dx.doi.org/10.1016/S1470-2045\(12\)70121-3](http://dx.doi.org/10.1016/S1470-2045(12)70121-3).
- [33] M.Z. Kiss, M.J. Daniels, T. Varghese, Investigation of temperature-dependent viscoelastic properties of thermal lesions in ex vivo animal liver tissue, *J. Biomech.* 42 (8) (2009) 959–966, <http://dx.doi.org/10.1016/j.jbiomech.2009.03.002>.
- [34] J. Lepetit, A theoretical approach of the relationships between collagen content, collagen cross-links and meat tenderness, *Meat Sci.* 76 (1) (2007) 147–159, <http://dx.doi.org/10.1016/j.meatsci.2006.10.027>.
- [35] N.T. Wright, J.D. Humphrey, Denaturation of collagen via heating: An irreversible rate process, *Annu. Rev. Biomed. Eng.* 4 (1) (2002) 109–128, <http://dx.doi.org/10.1146/annurev.bioeng.4.101001.131546>.
- [36] K. Hoyt, B. Castaneda, M. Zhang, P. Nigwekar, P. Anthony, S. Agnese, J.V. Joseph, J. Strang, D.J. Rubens, K.J. Parker, Tissue elasticity properties as biomarkers for prostate cancer, *Cancer Biomark.* 4 (2008) 213–225.
- [37] S. Woo, S.Y. Kim, J.Y. Cho, S.H. Kim, Shear wave elastography for detection of prostate cancer: a preliminary study, *Korean J. Radiol.* 15 (3) (2014) 346–355, <http://dx.doi.org/10.3348/kjr.2014.15.3.346>.
- [38] S. Müller, E. Niederleithinger, T. Bohlén, Reverse time migration: A seismic imaging technique applied to synthetic ultrasonic data, *Int. J. Geophys.* 2012 (2012) 1–7, <http://dx.doi.org/10.1155/2012/128465>.
- [39] G. Rus, N. Bochud, J.M. Melchor, L. Peralta, J. Chachio, M. Chlachio, A. Gomez, A.C. Ximenez, M. Alaminos, A. Campos, In-bioreactor ultrasonic monitoring of tissue mechanical properties, in: *ICU 2013 Proceedings*, 2013, pp. 657–661, http://dx.doi.org/10.3850/978-981-07-5938-4_P0298.
- [40] N. Whitmore, Iterative depth migration by backward time propagation, in: *SEG Expand. Abstr. 53rd Annu. Int. Meet.*, 1983, pp. 382–385, <http://dx.doi.org/10.1190/1.1893867>.
- [41] P. Farmer, I. Jones, H. Zhou, R. Bloor, M. Goodwin, Application of reverse time migration to complex imaging problems, *First Break* 24 (September) (2006) 64–73, <http://dx.doi.org/10.3997/1365-2397.24.9.27105>.
- [42] L. Zhou, F.G. Yuan, W.-J. Meng, A pre-stack migration method for damage identification in composite structures, *Smart Struct. Syst.* 3 (4) (2007) 439–454, <http://dx.doi.org/10.12989/ss.2007.3.4.439>.

- [43] R. Souchon, O. Rouvière, A. Gelet, V. Detti, S. Srinivasan, J. Ophir, J.Y. Chapelon, Visualisation of HIFU lesions using elastography of the human prostate in vivo: Preliminary results, *Ultrasound Med. Biol.* 29 (7) (2003) 1007–1015, [http://dx.doi.org/10.1016/S0301-5629\(03\)00065-6](http://dx.doi.org/10.1016/S0301-5629(03)00065-6).
- [44] E. Sapin-de Brosses, M. Pernot, M. Tanter, The link between tissue elasticity and thermal dose in vivo, *Phys. Med. Biol.* 56 (24) (2011) 7755–7765, <http://dx.doi.org/10.1088/0031-9155/56/24/005>.
- [45] F. Liu, G. Zhang, S.a. Morton, J.P. Leveille, An effective imaging condition for reverse-time migration using wavefield decomposition, *Geophysics* 76 (1) (2011) S29, <http://dx.doi.org/10.1190/1.3533914>.
- [46] T. Chen, B.-S. He, A normalized wavefield separation cross-correlation imaging condition for reverse time migration based on Poynting vector, *Appl. Geophys.* 11 (2) (2014) 158–166, <http://dx.doi.org/10.1007/s11770-014-0441-5>.
- [47] X. Jiang, L. Zhu, S. Hu, R. Huang, Three-dimensional reverse-time migration of teleseismic receiver functions using the phase-shift-plus-interpolation method, *Geophys. J. Int.* 217 (2) (2019) 1047–1057, <http://dx.doi.org/10.1093/gji/ggz066>.
- [48] O. Ovcharenko, V. Kazei, D. Peter, T. Alkhalifah, Variance-based model interpolation for improved full-waveform inversion in the presence of salt bodies, *Geophysics* 83 (5) (2018) R541–R551, <http://dx.doi.org/10.1190/geo2017-0575.1>.
- [49] R.G. Barr, R. Memo, C.R. Schaub, Shear wave ultrasound elastography of the prostate: initial results, *Ultrasound Q.* 28 (1) (2012) 13–20, <http://dx.doi.org/10.1097/RUQ.0b013e318249f594>.